Graduate University of Advanced Technology

Journal of Geological Remote Sensing

Journal homepage: https:// jgrs.kgut.ac.ir

Iranian Geological Remote Sensing Society

Structural and geological analysis of copper mineralization in the northern part of the Kerman copper belt, using remote sensing data

Mina Aboli *

M.Sc. student, Surgan Parseh Consulting Engineers, Kerman, Iran

Article Info

Keywords:
Geological structures
porphyry copper mineralization
hydrothermal alteration
SAM
lineament factor
Fry analysis

Abstract

Geological structures play a significant role in the emplacement of intrusive bodies, directing hydrothermal fluids, and forming mineral deposits. In this study, the relationship between geological lineaments and hydrothermal alterations with the location of copper deposits in the northern part of the Kerman copper belt has been determined using the Fry analysis method, photo lineament factor, and rose diagrams. First, the lineaments in the area were extracted by using satellite images (Landsat 9 and Sentinel 2), digital elevation models, and geological maps. Hydrothermal alteration of the region was also enhanced using the Spectra Angle Mapper (SAM) method on the Advanced Spaceborne Thermal Emission and Reflection Radiometer (ASTER) images. The spatial distribution of the deposits in the region was analyzed by Fry analysis. This investigation revealed that the dominant trend of deposits in the region is northwest-southeast. The map of the photo lineament factor (PF) of the faults showed that the average to higher values of PF are in good agreement with the known mineral deposits of the region. Rose diagrams also identified two dominant trends for the faults in the region. The comparison of the results obtained from Fry's analysis of the deposits and the rose diagrams of the faults demonstrated similar orientation for main faults and well-known deposits as a northwest-southeast strike in the study area.

*Corresponding author
Email: aboli.m614@gmail.com

https://doi.org/10.48306/jgrs.2023.398400.1003
Received 21 May 2023; Received in revised form 13 Aug. 2023; Accepted 5 Dec. 2023
Available online 5 Dec. 2023

1. Introduction

Porphyry copper deposits are one of the world's most important sources of copper production. Given that the Urumieh-Dokhtar magmatic belt hosts the majority of well-known porphyry copper deposits in Iran, there is good potential for reconnaissance and prospecting of these deposits. This magmatic belt is considered the most important geological location for Iran's magmatic and hydrothermal copper deposits. As the reconnaissance and prospecting of mineral deposits is a progressive science, modern remote sensing methods assist in its evolution and development. Hydrothermal alteration is one of the distinctive characteristics of porphyry copper deposits. Some types of hydrothermal alteration are the most important geological evidence for exploring porphyry copper deposits, which can be identified and mapped using multi-spectral remote sensing sensors due to their large extent. The intrusion of Miocene-aged bodies in the volcanic rocks of the study area is one of the main factors of extensive hydrothermal alteration and subsequent mineralization. Hydrothermal alteration typically exhibits centralized zoning in porphyry copper systems. The potassic alteration zone is located in the center of the system and passes outward toward the phyllic, argillic, and propylitic alteration zones (Lowell and Gilbert, 1970) (Figure 1). Specific minerals in each of the hydrothermal alteration zones are identified based on their unique spectral features in the visible to near-infrared range of the electromagnetic spectrum through the use of remote sensing sensors. It is a common and effective technique for locating the porphyry copper deposits.

Primary and secondary structural features such as faults and fractures control the extent of mineralization and hydrothermal alteration associated with porphyry copper deposits. They also play a very important role in placing intrusives and controlling mineralization in porphyry copper deposits. The structural features, such as faults and lineaments, which play a significant role in replacing hydrothermal solutions and mineralization, are crucial clues for mineral exploration (Honarmand, 2012). In addition to mapping hydrothermal alteration zones and lithological units, satellite remote sensing images can be utilized for structural studies related to various types of mineralization based on their spatial and spectral resolution.

Many statistical methods, such as fractal modeling (Mandelbrot, 1983) and Fry analysis (Fry, 1979), have been proposed to describe the spatial distribution of deposits and their spatial relationships with structures (such as faults and lineaments). Many researchers have also used Fry analysis to study the spatial pattern of known occurrences for mineral zoning and understanding geological events. Photo lineament Factor (PF) is another method that is used to analysis structures (Hardcastle, 1995). This method is often used to explore underground water and mineral deposits in crushed rocks. Calculating the linearity coefficient and studying the spatial distribution of linearities can be used in deposit exploration and the determination of areas with mineralization potential, as well as the exploration of storage and water transfer areas. In mineral exploration campaigns, fractures such as faults are considered as main linear structures that play an important role in forming mineral deposits. Thus, the number, length, number of intersections, and the strike of fracture sets are the main parameters for PF

analysis. Carranza (2009) investigated the spatial relationship between various geological features and mineral deposits. Accordingly, it was found that different geological features have a significant effect on the occurrence of mineral deposits at a particular geographical scale. Mehrabi et al. (2014) utilized point pattern and Fry analysis to investigate the distribution of hydrothermal deposits and demonstrated that structural controls play a major role in the distribution of deposits. Mohebi et al. (2015) used the Fry analysis method and rose diagrams to determine the relationship between the dominant trend of faults and copper mineralization in the Bondar Hanza deposit, Iran. Mirzababaei et al. (2016) identified lineaments and faults by using Landsat satellite images, in the Dehaj region, northern Kerman copper belt. They determined the trend of linear structures using the photo lineament factor (PF) and revealed the distribution of the deposits. It was concluded copper deposits in the Dehaj region were closely associated with linear structures and their regional intersections and followed distinct geological structures. Ahmadfaraj et al. (2019) analyzed the spatial relationships between geological structural features and copper deposits in the Saveh region, Iran using fractal modeling and the Fry analysis method. Accordingly, it was concluded that copper occurrences and deposits were associated with the major structural zones. This study aims to determine the relationship between structural features and alteration and the copper deposit using the Fry analysis method, photo lineament factor, and rose diagrams, in the northern portion of the Kerman copper belt, Iran.

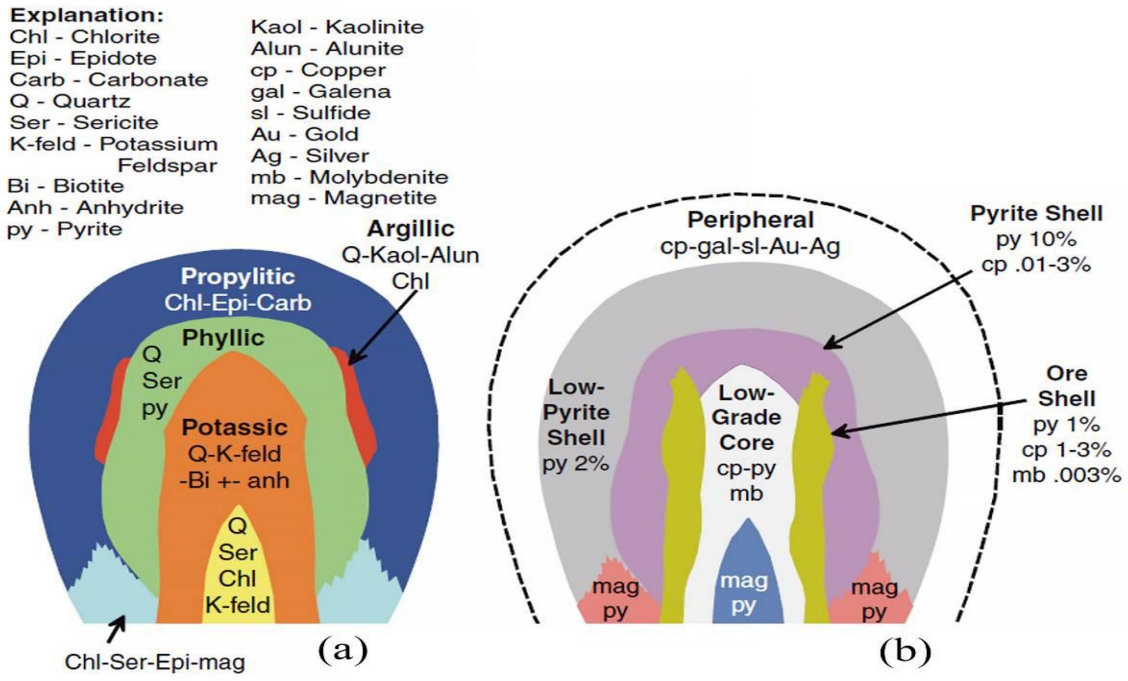

Figure 1. Model of hydrothermal alteration zones related to porphyry copper deposit (modified from Lowell and Guilbert, 1970, Sillitoe, 2010). (a) Schematic cross-section of hydrothermal alteration minerals and types, which include propylitic, phyllic, argillic, and potassic alteration. (b) Schematic cross-section of ores associated with each alteration type.

2. Geological setting

The Iran Cenozoic magmatic belt (ICMB), which is known as the Urumieh-Dokhtar magmatic belt (UDMB), is one of the most important metallogenic provinces in Iran. This magmatic complex, with a 50 to 80 km thickness, involves a significant volume of volcanic rocks. The central segment of the ICMB, also known as the Dehaj-Sarduiyeh magmatic belt or Kerman copper belt, hosts the majority of porphyry copper deposits (Ranjbar and Shahriari, 2006; Alimohammadi, 2015) (Figure 2a).

Kerman copper belt is characterized by a set of Cenozoic intrusive, pyroclastic, and sedimentary rocks. During the Early to Middle Eocene, in the Kerman copper belt, magmatic activity with acidic calc-alkaline pyroclastics, volcanic breccias, and Trachybasalt to Trachyandesite lava flows formed the Bahr-e-Aseman complex. Afterward, with the continuation and culmination of the magmatism process in the Upper Eocene, the Razak complex was formed. Finally, magmatic activity continued during the Oligocene with trachyandesite and trachybasalt lavas, creating the calc-alkaline Hezar volcanic complex. These three complexes are covered by carbonate rocks and sediments from the Upper Eocene to the Middle Miocene. During the Middle to Upper Miocene, the extensive magmatic and intrusive activity was replaced by the intrusion of older volcanic rocks, and intrusive bodies, and following the exit of this region from the water and the dominance of arid conditions (Dimitrijevic, 1973; Hassanzadeh, 1993). These intrusive bodies, mainly composed of diorite, quartz diorite, granodiorite, and granite, with porphyritic texture visible, represent the latest significant volcanic activity, including Dehaj, Mosahem, Bidkhan, and Aj activities, in the Kerman copper belt during the Late Miocene to Pliocene.

The study area is located in the north of Shahr-e-Babak, between 30°15’ to 30°45’ latitudes and 55°00’ to 55°30’ longitudes. This area is located northwest of the Dehaj-Sarduiyeh belt. The main rock assemblage of the area is composed of Eocene volcanic rocks and associated pyroclastics, cut by numerous intrusive bodies. The area also includes Cretaceous flysch units, Mélange ophiolite units, Miocene intrusive bodies, Hezar volcanic formations, and Quaternary sediments. This region’s volcanic activity has covered a large area from northwest to southeast with a varied combination of pyroxene and Trachyandesite, andesite basalt, tuff, agglomerate, volcanic breccias, and other pyroclastic rocks, along with small lenses of limestone. The porphyry copper mineralization in this area is of great importance, with notable deposits including Meiduk, Kader, Parkam, Chah-Firoozeh, Iju, Serenu, and Abdar, among others (Table 1). The Miocene intrusive bodies have cut through the volcanic rocks of this area, leading to the development of alteration halos of argillic, phyllic, and propylitic types. The major faults trend northwest to southeast and occasionally show a north-south trend (Honarmand, 2012) (Figure 2b).

Table 1 Summary of major copper deposits in the study area (Honarmand et al., 2011)

	Deposit	**Type of mineralization**	**Main alteration types**	**Main Altered minerals**
1	Kader	Porphyry	Phyllic, Argillic, Propylitic, Silicification	Pyrite, Chalcopyrite, Chalcocite, Covellite
2	Godekolvary	Porphyry	Argillic, Phyllic, Propylitic, Silicification	Pyrite, Chalcopyrite
3	Iju	Porphyry	Phyllic, Argillic, Potassic, Propylitic, Jarositization	Pyrite, Chalcopyrite, Chalcocite
4	Serenu	Porphyry	Phyllic, Argillic, Propylitic, Potassic	Pyrite, Chalcopyrite
5	Chahfiroozeh	Porphyry	Phyllic, Potassic, Propylitic	Malachite, Azurite, Chrysocolla, Pyrite, Chalcopyrite
6	Parkam	Porphyry	Phyllic, Argillic, Potassic, Propylitic, Jarositization, Silicification	Pyrite, Chalcopyrite, Malachite
7	Meiduk	Porphyry	Phyllic, Argillic, Potassic, Propylitic	Pyrite, Chalcopyrite, Chalcocite, Malachite
8	Abdar	Vein and Porphyry	Phyllic, Argillic, Propylitic	Pyrite, Chalcopyrite, Galena, Malachite
9	Palangi	Impregnation	Carbonatization, Propylitic, Chloritization, Sericitization, Silicification	Chalcopyrite, Malachite, Azurite, Chalcocite, Bornite
10	Chahmesi	Vein	Propylitic, Silicification	Chalcopyrite, Chalcocite, Sphalerite, Malachite, Azurite, Galena

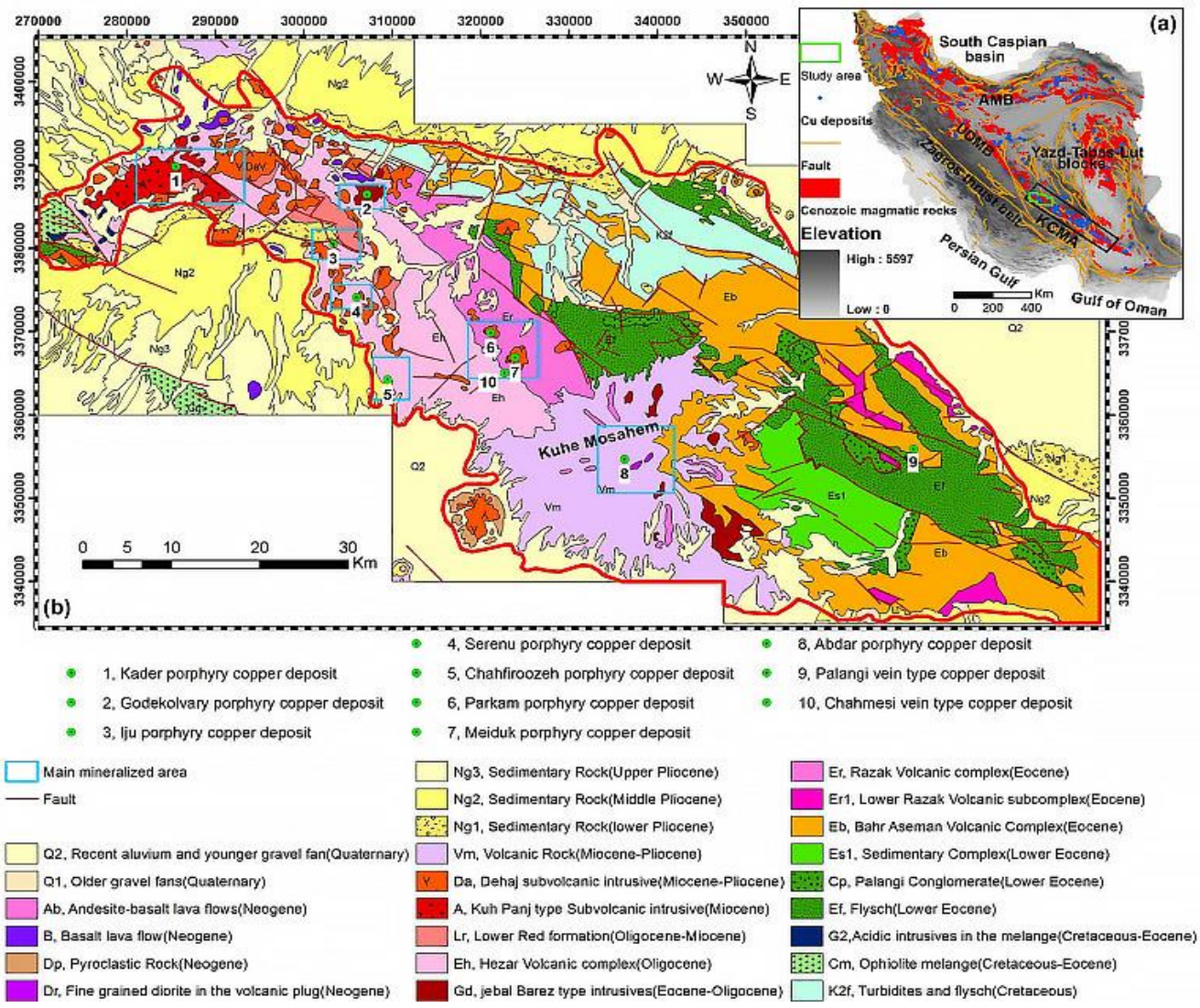

Fig 2. (a) Location map of Cenozoic volcanic belts, abbreviations used in the image AMB: Alborz Magmatic Belt, UDMB: Urumieh-Dokhtar Magmatic Belt, KMCA: Kerman Cenozoic Magmatic Arc; (b) Geological map of the studied area with the location of indicative copper deposits (Honarmand, 2012)

3. Materials and methods

3.1. Satellite data and pre-processing procedure

In this study, three ASTER L1B scenes were acquired on 13 July 2003, 21 May 2007, and 15 June 2007 (Table 2). The ASTER sensor, which was launched in December 1999, has three separate subsystems and a total of 14 spectral bands (Table 3). The visible near-infrared (VNIR) subsystem obtains optical images of three bands (0.52 to 0.86 micrometers) with a spatial resolution of 15 meters. The Shortwave Infrared (SWIR) subsystem scans six bands of optical images (1.60 to 2.43 micrometers) with a spatial resolution of 30 meters. The Thermal infrared (TIR) subsystem obtains five bands of optical images (8.12 to 11.65 micrometers) with a spatial resolution of 90 meters (Fujisada, 1995). The

crosstalk effect due to the light leakage from detector 4 on detectors in bands 5 to 9 was corrected using ENVI 5.3.1 software. The radiance Level 1B images were converted to surface reflectance using FLAASH atmospheric correction. Finally, all three images were geometrically corrected using the Landsat 9 image and ground control points (GCPs).

The Landsat 9 and Sentinel 2 satellite images were performed to highlight the faults and fractures in the study area. The Landsat 9 satellite was launched on 27 September 2021 and carries two sensors namely an Operational Land Imager (OLI-2) and Thermal Infrared Sensor (TIRS-2) (Table 3). The OLI-2 sensor has three bands in the VNIR range (with a spatial resolution of 30 meters), two bands in the SWIR range (with a spatial resolution of 30 meters), and the TIRS-2 sensor has two bands in the TIR range (with a spatial resolution of 100 meters). Band 8 of Landsat 9 also has a spatial resolution of 15 meters (Lemenkova et al., 2023). The used Landsat image was taken from Collection 2 Level 2 which required no radiometric and atmospheric corrections. Landsat nine bands were sharpened using its panchromatic band with a spatial resolution of 15 meters.

The Sentinel 2A satellite, which was launched on 23 January 2015, provides remote sensing data in 12 spectral bands in VNIR and SWIR regions. Sentinel 2 contains four visible and near-infrared (NIR) bands with a spatial resolution of 10 meters, six SWIR and red-edge bands with a spatial resolution of 20 meters, and three bands with a spatial resolution of 60 meters (Table 3). It has the capability of highlighting linear features and faults. Internal Average Relative Reflectance (IARR) correction was done on the Sentinel 2 data to convert radiance to relative reflectance (Ven der Werff and Ven der Meer, 2015).

Table 2 Technical specifications of satellite data that were used in the research

Product ID	Pre-processing level	Observation		Solar angle	
		Date	Time (UTC)	Azimuth	Elevation
ASTL1B-00307132003071404	L1B	13/07/2003	07:14:04	114.96	71.64
ASTL1B-00305212007071434	L1B	21/05/2007	07:14:34	121.78	72.45
ASTL1B-00306152007070834	L1B	15/06/2007	07:08:34	110.43	72.37
LC09-L2SP-161039-20220624-20220627-02-T1	L2SP	24/06/2022	06:51:01	103.29	68.58
S2A-MSIL1C-20180830T065621-N0206-R063-T40RCU-20180830T090947	L1C	28/08/2021	09:05:30	139.91	26.46

Table 3: Specifications of Landsat 9, Sentinel 2A, and ASTER sensors.

ASTER				Landsat 9				Sentinel 2A			
Band	Spectrum Covered	Central wave-lengths(µm)	Resolution (m)	Band	Spectrum Covered	Central wave-lengths(µm)	Resolution (m)	Band	Spectrum Covered	Central wave-lengths(µm)	Resolution (m)
1	VNIR	0.556	15	1	Coastal Aerosol	0.433	30	1	Coastal Aerosol	0.443	60
2	VNIR	0.661	15	2	Blue	0.482	30	2	Blue	0.490	10
3N	VNIR	0.807	15	3	Green	0.562	30	3	Green	0.560	10
3B	VNIR	0.804	15	4	Red	0.655	30	4	Red	0.665	10
4	SWIR	1.656	30	5	NIR	0.865	30	5	Vegetation Red Edge	0.705	20
5	SWIR	2.167	30	6	SWIR 1	1.610	30	6	Vegetation Red Edge	0.740	20
6	SWIR	2.209	30	7	SWIR 2	2.200	30	7	Vegetation Red Edge	0.783	20
7	SWIR	2.262	30	8	PAN	0.590	15	8	NIR	0.842	10
8	SWIR	2.336	30	9	Cirrus	1.375	30	8A	Vegetation Red Edge	0.865	20
9	SWIR	2.400	30	10	TIRS 1	10.800	100	9	Water vapour	0.945	60
10	TIR	8.291	90	11	TIRS 2	12.000	100	10	SWIR-Cirrus	1.375	60
11	TIR	8.634	90					11	SWIR	1.610	20
12	TIR	9.075	90					12	SWIR	2.190	20
13	TIR	10.657	90								
14	TIR	11.318	90								

3.2. Spectral Angle Mapper method (SAM)

The spectral angle mapper was used to enhance the different alteration zones in the study area. SAM identifies the desired target(s) by calculating the similarity between the spectrum of the image and the reference spectrum by calculating angles between the two spectra after converting them to vectors (Kruse et al. 1993). The smaller angle means more similarity between the two spectra. The brightest pixels

deviate from the standard the least, while the darkest pixels deviate the most (Nazeer et al., 2014; Kaufman, 1988). Three types of reference spectra including image, digital library, and field samples spectra are generally used in the SAM algorithm (Honarmand et al., 2018). This study used the United States Geological Survey (USGS) spectral library as a reference for the spectra.

3.3. Filtering and Lineament Extraction

To detect faults and structural fractures on satellite images, the visible bands of Sentinel 2A with a spatial resolution of 10 meters and the color composition of Landsat 9 bands with a spatial resolution of 15 meters were used in Arc GIS software. Moreover, directional filters with a 3*3 kernel in two different directions by directional filter (northwest-southeast and northeast-southwest) and highpass filter were applied to the Landsat 9 images. These filtered images were then combined in RGB color composition. Finally, the result of filtering, the geological map (1:100000 scale), and the digital elevation model (DEM) of the area with a resolution of 12.5 meters and 30 meters were used to prepare a map of the faults in the study area based on visual interpretation Arc GIS software.

3.4. Photo lineament Factor Map (PF) and Rose Diagram

Drawing rose diagrams usually is a simple and effective technique for determining the main trends of faults. The faults map of the study area was initially applied for analysis of structural trends using the rose diagrams in the study area. After identifying the dominant trends of lineaments, the photo lineament factor (PF) was prepared to investigate the spatial distribution of lineaments to explore deposits and determine the areas with high mineralization potential (Honarmand and Ranjbar, 2005). PF determines the intensity of faults and fragments in the region. This method initially proposed by Hardcastle (1995) can be employed to locate underground water in brittle and fractured rocks, and can also be useful for exploring porphyry deposits (Honarmand and Ranjbar, 2005).

The number, length, and intersection of lineaments were calculated to determine the PF using a 5000×5000-meter grid on the satellite images. Then, the PF values were calculated using the following equation (Hardcastle 1995):

$$PF=(a/A) +(b/B) +(c/C)$$

where a represents the number of lineaments in each cell, A is their average across the entire map, b is the length of lineaments in each cell, B is their average across the entire map, c is the number of lineament intersections in each cell, and C is their average across the entire map. Finally, the PF map was prepared using the ArcGIS software through the interpolation method (IDW).

3.5. Fry Analysis

There are many known important deposits including nineteen vein-type and porphyry copper deposits in the study area (Figure 3 and Table 4). These point data, which have a certain spatial distribution, were analyzed using the Fry method in the DotProc software. Fry analysis is a geometric method for analyzing spatial point data and studying the mineralization trend. This method considers each point as the center and moves other points accordingly. In the first step, all points are plotted on a sheet and numbered. Then, on a transparent sheet, a point is considered the center point and is sequentially placed on all points, and other points are drawn based on it. This procedure is applied to all points, and for every n point, n^2-n additional points are generated. The resulting image is a Fry diagram depicting the spatial distribution of the original data, from which a rose diagram can also be created, whose analysis is simpler and more reliable than that of the Fry diagram itself (Ige et al., 2022; Ahmadfaraj et al., 2019).

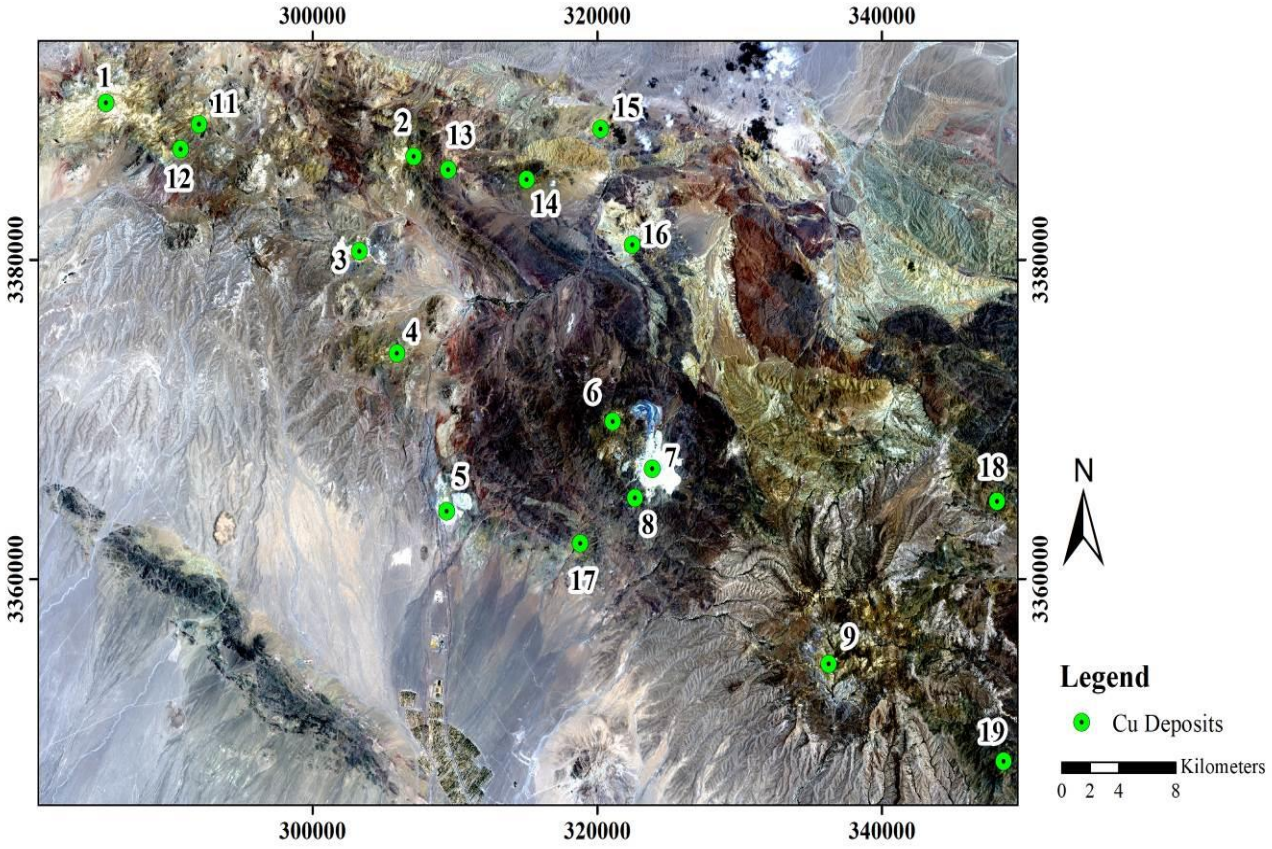

Fig. 3. Location of known vein-type and porphyry copper deposits in the study area on the Landsat 9 image

Table 4: Location of porphyry copper deposits in the study area.

Number	**Name**	**Type**	**X**	**Y**
1	Kader	Vein and Porphyry	285503	3389840
2	Gode Kolvary	Vein and Porphyry	307128	3386478
3	Iju	Porphyry	303315	3380542
4	Serenu	Porphyry	305954	3374148
5	Chah Firoozeh	Vein and Porphyry	309441	3364244
6	Parkam	Porphyry	321121	3369859
7	Meiduk	Porphyry	323885	3366900
8	Chah Mesi	Vein	322677	3365076
9	Abdar	Vein and Porphyry	336271	3354694
11	Sineh Khar	Vein and Porphyry	292046	3388508
12	Kuhe Zamzu	Vein and Porphyry	290739	3386925
13	East Gode Kolvary	Vein and Porphyry	309545	3385636
14	Kabudan	Vein	315045	3385040
15	Tizerj	Vein	320258	3388195
16	Kankuh	-----	322466	3380934
17	Kuhe Pirgol	Vein	318809	3362235
18	NHameddin	Vein	348086	3364858
19	Chenar	Vein and Impregnation	348530	3348579

4. Results and Discussion

Today, remote sensing is used in mineral exploration campaigns for mapping hydrothermal alterations, geology, and geological structures. This study examined influential information data to determine the relationship between copper mineralization, the geological structures, and hydrothermal alterations. The hydrothermal alterations such as phyllic, argillic, and propylitic alterations in the study area were highlighted using the SAM method (Figure 4). The reference spectra for executing the SAM algorithm were obtained from the USGS digital spectral library. By comparing Figures 3 and 4, known copper deposits in the study area such as Kader, Godklovary, Iju, Serenu, ChahFiroozeh, Parkam, Meiduk, Abdar, Palangi, and ChahMesi were well-suited with the discriminated hydrothermal alteration map.

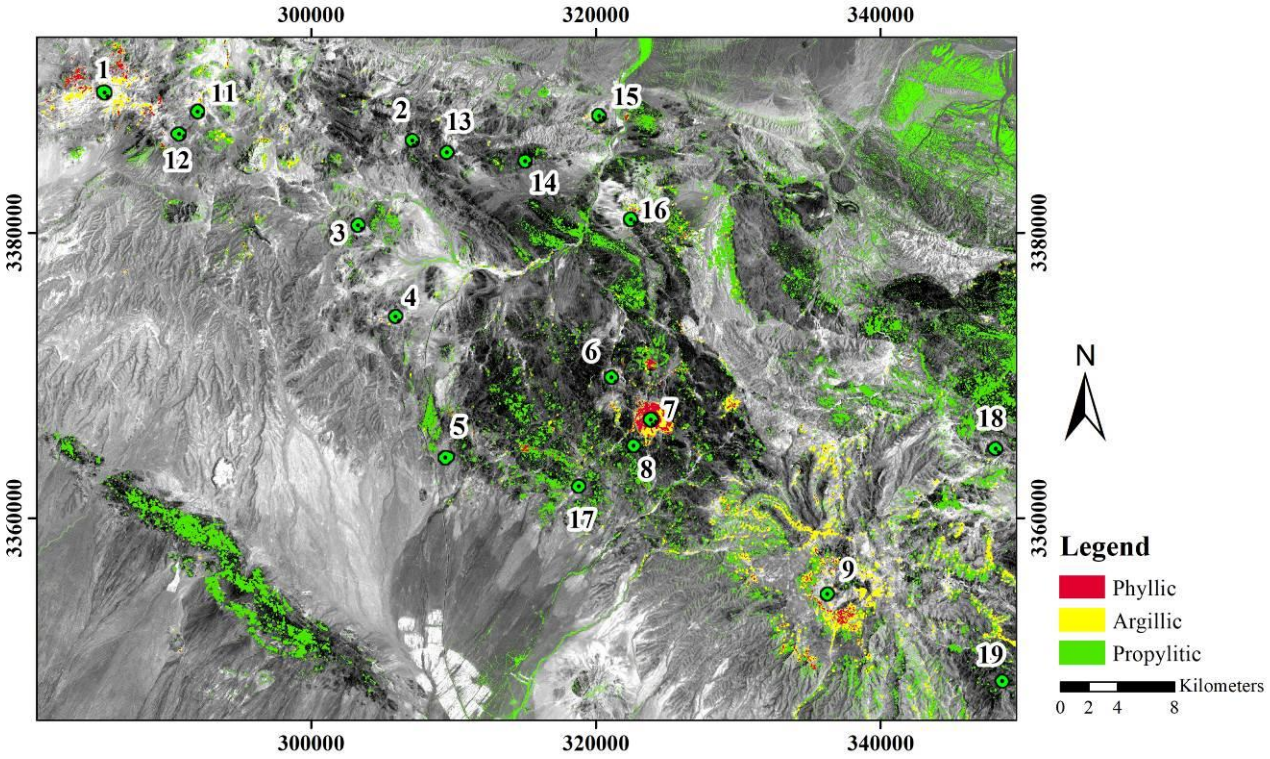

Fig. 4. SAM result presenting the hydrothermal alteration zones in the study area.

The discriminated faults and fractures of the study area are shown in Figure 5. Based on Figure 5b, most of the faults and fractures exhibit a northeast-southwest trend. The northwest-southeast trend was also recognized from main faults and fractures in the study area (Figure 5c). Secondary faults and fractures present a northeast-southwest trend (Figure 5d).

The Fry analysis method was used to determine the trend and investigate the distribution of deposits in the study area. The result was then presented as a rose diagram in Figure 5e to facilitate identifying the dominant mineralization trends. The rose diagram of Fry analysis indicates the deposits distributed in the northwest-southeast trend (Figure 5e).

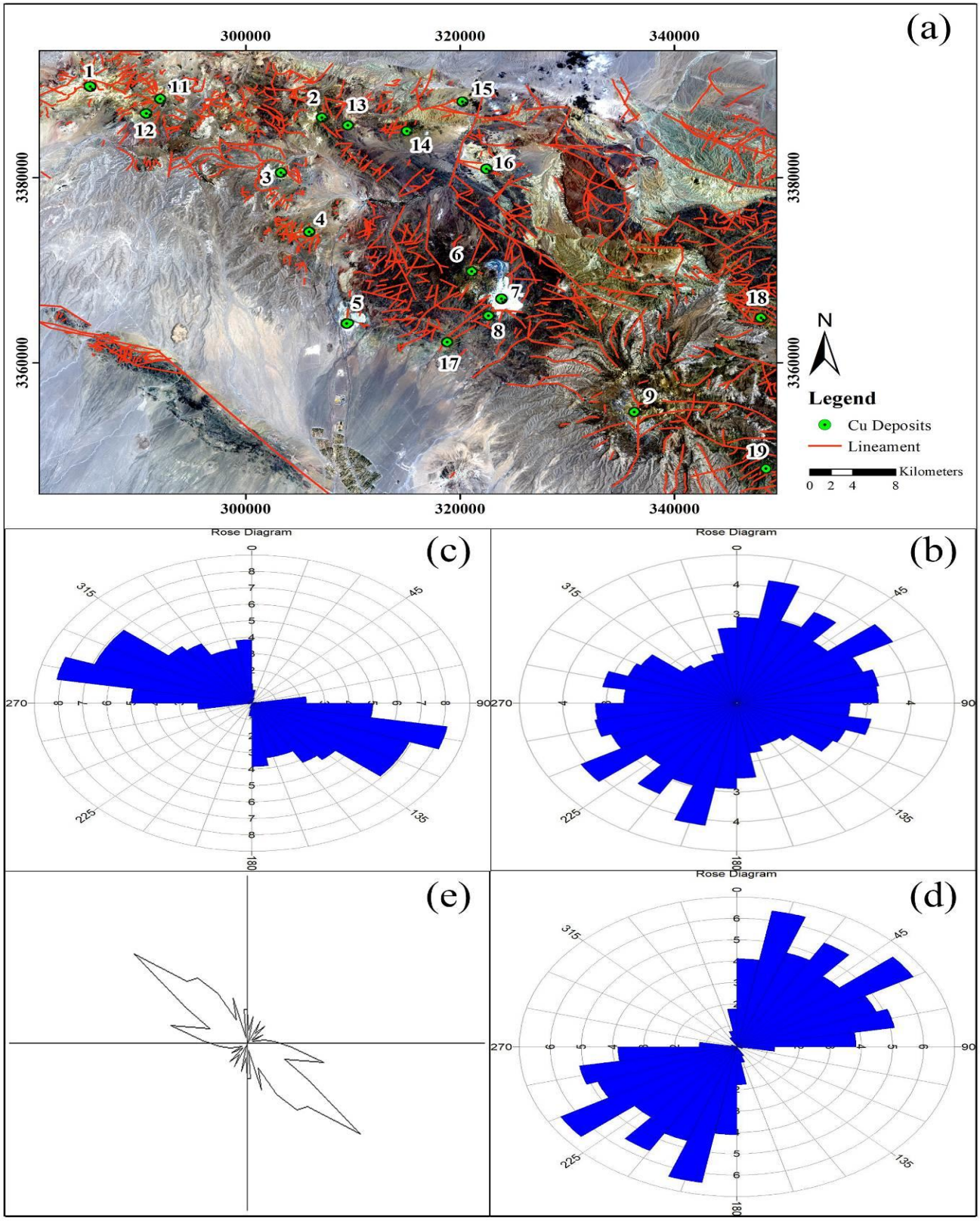

Fig. 5. (a) Map of lineaments and deposits in the study area on Landsat 9 image; (b) Rose diagram of all faults; (c) Rose diagram of main faults; (d) Rose diagram of secondary faults; (e) Fry diagram of deposits in the study area.

After extracting faults and linear structures, the PF map was prepared to analyze the geological structures. Considering the role of faults and structural lineaments in circulating and distributing hydrothermal fluids, high PF values can offer a higher probability of Cu-occurring mineralization. In some areas with high PF, a certain amount of distance from the ore deposits can be observed (Figure 6). One of the main reasons for the lack of coherence may be the large size of the cells (5000×5000-meter grid) considered to obtain PF. Also, another reason for the lack of coordination can be the exit of a large amount of ore-forming fluids and elements from the magma system and the loss of magma ore-making value due to the abundant presence of magma before its evolution and subtraction to form alterations and copper deposits (Mirzababaei et al., 2016). However, by studying the PF map and comparing it with mineralized areas and hydrothermal alterations, it was discovered that there is a reasonably strong correlation between high PF values and the location of deposits and hydrothermal alteration zones (Figure 6).

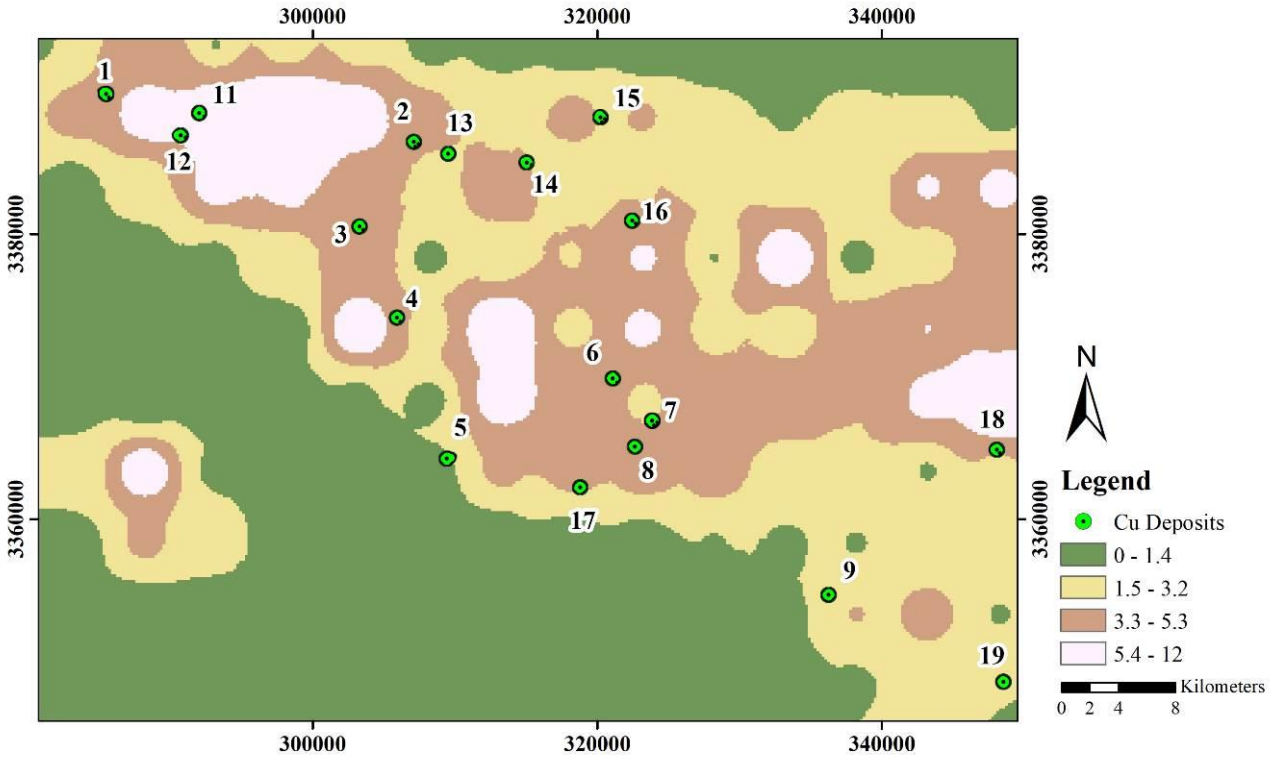

Fig. 6. PF map showing a good correlation between areas with medium to high PF and the location of copper deposits.

5. Conclusion

Fractures play an important role in circulating and distributing ore-forming fluids. hydrothermal alterations were highlighted using the ASTER data and SAM method in this research. The faults and geological structures in the area were extracted using Landsat 9, Sentinel 2, geological maps, DEM

models, and directional filter images. The Fry method was applied to analyze 19 areas deemed known copper deposits in the study area. The rose diagram of Fry analysis showed a dominant northwest-southeast trend for known copper deposits. The majority of deposits are located in the regions with moderate to high PF values according to the PF map. The rose diagram of fractures and faults also showed two dominant trends of northwest-southeast and northeast-southwest. These results show that the main faults of the region are in sync with the mineralization process of the region. According to the comparison of the results of Fry's analysis for the distribution of deposits and the maps specifying structural trends and faults, it was found that linear structures play a very important and controlling role in the spatial distribution of deposits and It can receive more attention in other exploratory operations and deposit modeling.

6. References

Ahmadfaraj M, Mirmohammadi M, Afzal P, Yasrebi AB, Carranza EJ. Fractal modeling and fry analysis of the relationship between structures and Cu mineralization in Saveh region, Central Iran. Ore Geology Reviews. 2019; 107:172-85.

Alimohammadi M, Alirezaei S, Kontak DJ. Application of ASTER data for exploration of porphyry copper deposits: A case study of Daraloo–Sarmeshk area, southern part of the Kerman copper belt, Iran. Ore Geology Reviews. 2015; 70:290-304.

Carranza EJ. Controls on mineral deposit occurrence are inferared from analysis of their spatial pattern and spatial association with geological features. Ore Geology Reviews. 2009 ;35(3-4):383-400.

Dimitrijevic MD. Geology of Kerman region: institute for Geological and Mining Exploration and Investigation of Nuclear and other mineral raw material, Beograd—Yugoslavia, Iran Geol. Survey Rept Yu/52. 1973.

Fry N. Random point distributions and strain measurement in rocks. Tectonophysics. 1979 ;60(1-2):89-105.

Fujisada H. Design and performance of ASTER instrument. InAdvanced and next-generation satellites 1995(Vol. 2583, pp. 16-25). SPIE.

Hardcastle KC. Photolineament factor: a new computer-aided method for remotely sensing the degree to which bedrock is fractured. Photogrammetric Engineering and Remote Sensing. 1995 ;61(6):739-46.

Hassanzadeh J. Metalogenic and tectonomagmatic events in SE sector of the Cenozoic activecontinental marfin of central Iran (Shahre-Babak, Kerman Province) [Unpublished PhD Thesis]. California: Los Angeles; 1993.

Honarmand M, Ranjbar H, Shahabpour J. Application of spectral analysis in mapping hydrothermal alteration of the Northwestern Part of the Kerman Cenozoic Magmatic Arc, Iran. Journal of Sciences, Islamic Republic of Iran. 2011 ;22(3):221-38.

Honarmand M, Ranjbar H. Application of different image processing techniques on ETM^+ images for exploration of porphyry and vein type copper mineralizations in Kuh-e-mamzer and Kuh-e-panj areas, Kerman province, Geosciences, 2005; 110-127.

Honarmand, M., Ranjbar, H., Shahriari, H., & Naseri, F.. Evaluating the effect of using different reference spectra on SAM classification results: an implication for hydrothermal alteration mapping. Journal of Mining and Environment, 2018, 9(4), 981-997.

Honarmand M. Mineral potential modeling of Kerman metallogenic copper belt using GIS [PhD Thesis]. Kerman: Shahid Bahonar Uni.; 2012.

Ige OO, Tende AW, Bale RB, Gajere JN, Aminu MD. Spatial mapping of hydrothermal alterations and structural features for gold and cassiterite exploration. Scientific African. 2022 ;17:e01307.

Kruse FA, Lefkoff AB, Boardman JW, Heidebrecht KB, Shapiro AT, Barloon PJ, Goetz AF. The spectral image processing system (SIPS)—interactive visualization and analysis of imaging spectrometer data. Remote sensing of the environment. 1993 ;44(2-3):145-63.

Lemenkova P, Debeir O. Recognizing the Wadi Fluvial Structure and Stream Network in the Qena Bend of the Nile River, Egypt, on Landsat 8-9 OLI Images. Information. 2023 ;14(4):249.

Lowell JD, Guilbert JM. Lateral and vertical alteration-mineralization zoning in porphyry ore deposits. Economic geology. 1970 ;65(4):373-408.

Mandelbrot BB. The fractal geometry of nature.638th ed. New York: Freeman; 1982.

Mehrabi B, Ghasemi SM, Tale FE. Structural control on epithermal mineralization in the Troud-Chah Shirin belt using point pattern and Fry analyses, north of Iran. Geotectonics. 2015 ;49:320-31.

Mirzababaei G, Shahabpour J, Zarasvandi A, Hayatolgheyb SM. Structural controls on Cu metallogenesis in the Dehaj area, Kerman porphyry copper belt, Iran: a remote sensing perspective. Journal of Sciences, Islamic Republic of Iran. 2016 ;27(3):253-67.

Mohebi A, Mirnejad H, Lentz D, Behzadi M, Dolati A, Kani A, Taghizadeh H. Controls on porphyry Cu mineralization around Hanza Mountain, south-east of Iran: An analysis of structural evolution from remote sensing, geophysical, geochemical and geological data. Ore Geology Reviews. 2015 ;69:187-98.

Nazeer M, Nichol JE, Yung YK. Evaluation of atmospheric correction models and Landsat surface reflectance product in an urban coastal environment. International journal of remote sensing. 2014 ;35 (16):6271-91.

Ranjbar, H., & Shahriari, H. (2006). Comparison of ETM+ and ASTER data for hydrothermal alteration mapping in the central part of the Dehaj-Sarduyeh belt, Kerman Province. Iran. J. Crystallogr. Mineral, 14(2), 367-382.

Sillitoe RH. Porphyry copper systems. Economic geology. 2010;105(1):3-41.

Van der Werff H, Van der Meer F. Sentinel-2 for mapping iron absorption feature parameters. Remote sensing. 2015 ;7(10):12635-53.